Recent Advances in Electron Momentum Spectroscopy *

Erich Weigold

Electronic Structure of Materials Centre, School of Physical Sciences, The Flinders University of South Australia, Adelaide 5001, Australia

Z. Naturforsch. **48a**, 371–389 (1993); received March 28, 1992

The flexibility of the (e, 2e) technique or "electron momentum spectroscopy" (EMS) in obtaining information on the electronic structure of atoms, molecules, and solids is demonstrated. High-resolution EMS measurements for argon, including the first measurements of momentum profiles belonging to the $^2P^0$ and $^2D^e$-manifolds, are used to demonstrate the technique for atomic targets. The d-wave transitions in argon are entirely due to initial-state correlations. The first (e, 2e) measurements on an excited target, and also on an oriented target, are discussed. Sodium atoms are pumped to the $m_l = +1$ state of the excited 3p-state by σ^+-light from a laser. The (e, 2e) measurements on this excited state are in excellent agreement with the momentum density given by the 3p ($m_l = 1$) Hartree-Fock wavefunction. The recent measurements of the valence-electron momentum distributions for ethyne, as well as some earlier results for water, are used as an example of the application of EMS to the study of molecules. The application of the EMS technique to measure spectral momentum densities in condensed-matter targets is demonstrated by some recent results on amorphous carbon.

Key words: Electron momentum densities; Electron momentum spectroscopy; Wavefunction mapping; Binding energies.

1. Introduction

An electron-impact ionising collision in which the momenta of the incident and two emitted electrons are determined is called an (e, 2e) collision. Such collisions are capable of revealing a rich variety of information. Depending on the kinematics employed, it is possible to investigate in detail either the dynamics of the ionising collision [1–3] or to elucidate the structure of the target and ion [4]. When used for structure determinations, the technique has been variously called electron coincidence spectroscopy, binary (e, 2e), or electron momentum spectroscopy (EMS). For EMS the kinematics are chosen so that the incident and exit electron energies are high and that the momentum transfer by the incident electron to the target is also high. High energies mean that there is very little distortion of the free electron waves and that they can be well represented by plane waves, and high momentum transfer implies close electron–electron collisions, i.e. binary encounter.

Under EMS conditions the (e, 2e) reaction measures electron separation (binding) energies to final ion states and maps out one-electron momentum densities for the transitions to these final states. In the present work I will first briefly outline the notation and theoretical background to EMS before discussing some recent applications to the study of atoms, molecules, and thin films.

2. Notation and Theoretical Background

In EMS the momenta $\boldsymbol{k}_0$, $\boldsymbol{k}_s$ and $\boldsymbol{k}_e$ of the incident, scattered, and ejected electron are all observed, with the outgoing electrons detected in coincidence. (We will use the terms "scattered" and "ejected" although the two emitted electrons are, of course, indistinguishable.) The quantities of primary interest are related to the observed momenta and corresponding kinetic energies. They are the ion recoil momentum

$$\boldsymbol{p} = \boldsymbol{k}_0 - \boldsymbol{k}_s - \boldsymbol{k}_e \tag{1}$$

and the electron separation (or binding) energy

$$\varepsilon_f = E_0 - E_s - E_e\,, \tag{2}$$

where ε_f is the energy difference between the initial target state i and final state f of the ion. The final ion state may be in the continuum, i.e. further ionisation may occur. The kinetic energies of the target and recoiling ion have been neglected.

* Presented at the Sagamore X Conference on Charge, Spin and Momentum Densities, Konstanz, Fed. Rep. of Germany, September 1–7, 1991.

Reprint requests to Prof. Dr. Erich Weigold, Director, Research School of Physical Sciences a Engineering, Australian National University, Canberra, ACT, 0200 Australia.

0932-0784 / 93 / 0100-0371 $ 01.30/0. – Please order a reprint rather than making your own copy.

The differential cross-section for an ionising reaction is given in atomic units ($\hbar = m = e = 1$) by

$$\frac{d^5\sigma}{d\hat{k}_s\, d\hat{k}_e\, dE_s} = (2\pi)^4 \left(\frac{k_s\, k_e}{k_0}\right) \sum_{av} |T(\varepsilon_f; \boldsymbol{k}_e, \boldsymbol{k}_s, \boldsymbol{k}_0)|^2 . \quad (3)$$

Here $T(\varepsilon_f; \boldsymbol{k}_s, \boldsymbol{k}_e, \boldsymbol{k}_0)$ is the amplitude for the reaction leading to the ion state f, $\sum_{av}$ denotes a sum over final- and average over initial-state degeneracies.

The ionisation amplitude may be written in terms of distorted waves $\chi^{(\pm)}$ for each fast electron [4],

$$T(\varepsilon_f; \boldsymbol{k}_s, \boldsymbol{k}_e, \boldsymbol{k}_0) \equiv \langle \chi^{(-)}(\boldsymbol{k}_s)\, \chi^{(-)}(\boldsymbol{k}_e) f | \tau | i\, \chi^{(+)}(\boldsymbol{k}_0) \rangle . \quad (4)$$

The operator τ describes the collision exactly in the distorted-wave representation. At high enough momentum transfer $\boldsymbol{K} = \boldsymbol{k}_0 - \boldsymbol{k}_s$, the momentum is transferred to the outgoing electrons only by a collision with a moving target electron. In this binary-encounter approximation the operator τ depends only on the coordinates of the two outgoing electrons and not on those of the remaining particles constituting the ion. In this case it commutes with the ion state f. Introducing a complete set of plane-wave states $|\boldsymbol{q}\rangle$ we get

$$T(\varepsilon_f; \boldsymbol{k}_s, \boldsymbol{k}_e, \boldsymbol{k}_0) \quad (5)$$
$$= \int d^3q \, \langle \chi^{(-)}(\boldsymbol{k}_s)\, \chi^{(-)}(\boldsymbol{k}_e) | \tau | \boldsymbol{q}\, \chi^{(+)}(\boldsymbol{k}_0) \rangle \, \langle f | a(\boldsymbol{q}) | i \rangle .$$

Thus in the binary-encounter approximation the (e, 2e) reaction becomes a probe for the target-ion-overlap $\langle f | a(\boldsymbol{q}) | i \rangle$ resulting from the annihilation of an electron of momentum $\boldsymbol{q}$ in the target state $|i\rangle$, with a probe factor

$$P_{seo}(\boldsymbol{q}) \equiv \langle \chi^{(-)}(\boldsymbol{k}_s)\, \chi^{(-)}(\boldsymbol{k}_e) | \tau | \boldsymbol{q}\, \chi^{(+)}(\boldsymbol{k}_0) \rangle \quad (6)$$

describing distortions from a perfect probe.

In the impulse approximation, τ is the free electron–electron amplitude t_s. If the energies are so high that $\chi^{(\pm)}(\boldsymbol{k})$ can be well described as plane waves, then we have the plane-wave impulse approximation (PWIA), and

$$P_{seo}(\boldsymbol{q}) = \langle \boldsymbol{k}_s \boldsymbol{k}_e | t_s | \boldsymbol{q} \boldsymbol{k}_0 \rangle = \langle \boldsymbol{k}' | t_s | \boldsymbol{k} \rangle \, \delta(\boldsymbol{q} + \boldsymbol{p}), \quad (7)$$

where $\boldsymbol{k}' = \frac{1}{2}(\boldsymbol{k}_s - \boldsymbol{k}_e)$ and $\boldsymbol{k} = \frac{1}{2}(\boldsymbol{k}_0 - \boldsymbol{q})$ and $\boldsymbol{p}$ is the measured ion recoil momentum, (1). The momentum of the annihilated target electron is therefore equal and opposite to the ion recoil momentum, $\boldsymbol{q} = -\boldsymbol{p}$.

Thus the PWIA differential cross-section is given by

$$\frac{d^5\sigma}{d\hat{k}_s\, d\hat{k}_e\, dE_s} = (2\pi)^4 \left(\frac{k_s\, k_e}{k_0}\right) f_{ee} \sum_{av} |\langle f | a(\boldsymbol{q}) | i \rangle|^2 , \quad (8)$$

where the e–e collision factor f_{ee} is the absolute square of the half-off-shell Coulomb t-matrix element of (7), summed and averaged over final and initial spin states. The kinematics usually employed in EMS studies is the noncoplanar symmetric one in which $k_e = k_s$, $\theta_e = \theta_s \approx 45°$, and the out-of-plane azimuthal angle $\phi = \pi - \phi_e - \phi_s$ is varied to vary $\boldsymbol{q}$. This geometry, as well as having experimental advantages such as symmetry about the $\phi = 0$ plane for unpolarised electrons and targets, also maximises the momentum transfer K and keeps its magnitude constant as ϕ is varied. Large K ensures the validity of the binary-encounter approximation. In the noncoplanar-symmetric geometry, f_{ee} is essentially constant and the cross-section is simply proportional to the square of the target-ion overlap amplitude resulting from the annihilation of an electron of momentum $\boldsymbol{q}$ in the target state $|i\rangle$. This is the EMS region of the (e, 2e) reaction.

In a normal experiment, magnetic degeneracies are not resolved. The consequent sum and average removes the dependence of the cross-sections on magnetic quantum numbers, and the initial-state average results in the division by the magnetic multiplicity of the initial target state $2J_i + 1$. It is possible to select magnetic quantum numbers in the initial target state by, e.g., laser excitation thereby orienting or aligning the target. This case will be discussed later.

For EMS of molecules, final rotational and vibrational states are generally not resolved. Using the Born-Oppenheimer approximation, they are eliminated by closure in the cross-section expression [4, 5]. The target temperature is usually so low that the initial state is in its vibrational ground state. Averaging over the initial rotational states with normalised Maxwellian weights is equivalent to the spherical average over the direction $\hat{\boldsymbol{q}}$. The vibrational average is sufficiently represented by taking the electronic wavefunctions calculated at the equilibrium positions of the nuclei in the target [5, 6].

The PWIA differential cross-section for (e, 2e) on a closed-shell molecule in EMS conditions is directly proportional to the spherically averaged square of the electronic overlap,

$$\frac{d^5\sigma}{d\hat{k}_e\, d\hat{k}_s\, dE_s} = (2\pi)^4 \frac{k_e\, k_s}{k_0} f_{ee} (4\pi)^{-1} \int d\hat{\boldsymbol{q}} \, |\langle f | a(\boldsymbol{q}) | i \rangle|^2 . \quad (9)$$

The information about the target and ion structure is contained in the electronic overlap.

The weak-coupling expansion of the target-ion overlap is

$$\langle f | a(\boldsymbol{q}) | i \rangle = \sum_l \langle f | l \rangle \langle l | a(\boldsymbol{q}) | i \rangle , \quad (10)$$

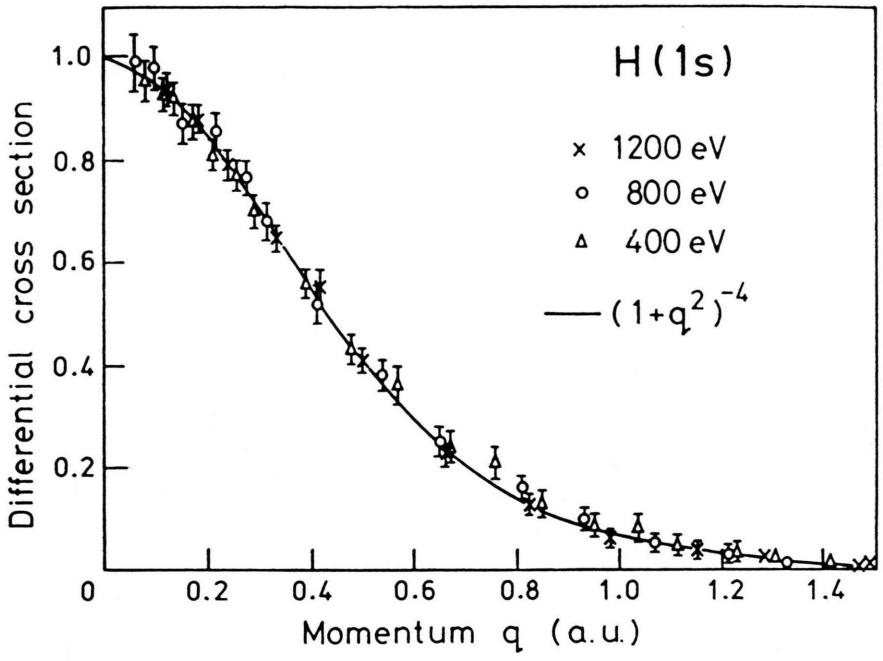

Fig. 1. The measured EMS momentum profile for atomic hydrogen at different total energies [7] compared with $|\psi_{1s}(q)|^2$ (solid curve).

where the orthonormal basis states $|l\rangle$ are linear combinations of configurations formed by annihilating one electron in a target state. Generally only a single hole state $|j\rangle$ contributes to the expansion in (10). We can define an experimental orbital $\psi_j(\boldsymbol{q})$ by

$$\psi_j(\boldsymbol{q}) \equiv \langle j|\, a(\boldsymbol{q})\, |\mathrm{i}\rangle\,, \tag{11}$$

and the spectroscopic factor, which is the probability of the one-hole configuration $|j\rangle$ contributing to the weak-coupling expansion of the ion state $|\mathrm{f}\rangle$, by

$$S_\mathrm{f}^{(j)} = |\langle \mathrm{f}|j\rangle|^2 . \tag{12}$$

The form used for the differential cross-section in the PWIA is therefore

$$\frac{\mathrm{d}^5\sigma}{\mathrm{d}\hat{\boldsymbol{k}}_\mathrm{e}\,\mathrm{d}\hat{\boldsymbol{k}}_\mathrm{s}\,\mathrm{d}E_\mathrm{s}} = (2\pi)^4 \frac{k_\mathrm{e}\,k_\mathrm{s}}{k_0} f_\mathrm{ee}\, S_\mathrm{f}^{(j)} (4\pi)^{-1} \int \mathrm{d}\hat{\boldsymbol{q}}\, |\psi_j(\boldsymbol{q})|^2 . \tag{13}$$

Thus momentum profiles for ion states f belonging to the same manifold j have the same shape, determined by the orbital $\psi_j(\boldsymbol{q})$. If the initial target state $|\mathrm{i}\rangle$ can be described by its Hartree-Fock wavefunction, $\psi_j(\boldsymbol{q})$ is simply the Hartree-Fock orbital $\phi_j(\boldsymbol{q})$.

The spectroscopic factors obviously obey the sum rule

$$\sum_{\mathrm{f}\in j} S_\mathrm{f}^{(j)} = 1\,. \tag{14}$$

The energy ε_j for the one-hole configuration $|j\rangle$, the orbital energy, is defined by

$$\varepsilon_j = \langle j|\, H_\mathrm{ion}\, |j\rangle = \sum_\mathrm{f} \langle j|\, H_\mathrm{ion}\, |\mathrm{f}\rangle\langle \mathrm{f}|j\rangle = \sum_{\mathrm{f}\in j} S_\mathrm{f}^{(j)}\, \varepsilon_\mathrm{f}\,. \tag{15}$$

Thus the orbital energy ε_j is the centroid of the energies ε_f of ion states belonging to the manifold j.

For a crystal the average over initial degeneracies does not involve the spherical averaging that arises in gas targets due to the rotational motion. The structure factor in (8) is replaced by [4, 5]

$$|\langle \mathrm{f}|\, a(\boldsymbol{q})\, |\mathrm{i}\rangle|^2 = |\psi_k^\alpha(\boldsymbol{q})|^2 = \sum_{\alpha \boldsymbol{B}} |\psi_k^\alpha(\boldsymbol{k}+\boldsymbol{B})|^2\, \delta(\boldsymbol{q}, \boldsymbol{k}+\boldsymbol{B})\, \delta(\varepsilon - \varepsilon^\alpha(\boldsymbol{q}))\,, \tag{16}$$

where α is the band label, $\boldsymbol{B}$ a reciprocal-lattice vector, $\boldsymbol{k}$ the electron quasimomentum, and $-\boldsymbol{q}$ the recoil momentum as before. The (e, 2e) reaction can therefore be used to map the momentum density of electrons in the band as well as the dispersion law $\varepsilon^\alpha = \varepsilon^\alpha(\boldsymbol{k})$, since the cross-section is finite only for $\boldsymbol{q} = \boldsymbol{k} + \boldsymbol{B}$. For a fixed energy the cross-section will therefore be finite at a discrete set of values of $\boldsymbol{q}$ with an envelope given by (16). A change of energy will map the momentum-space wavefunction of the band at a different set of $\boldsymbol{q}$ values.

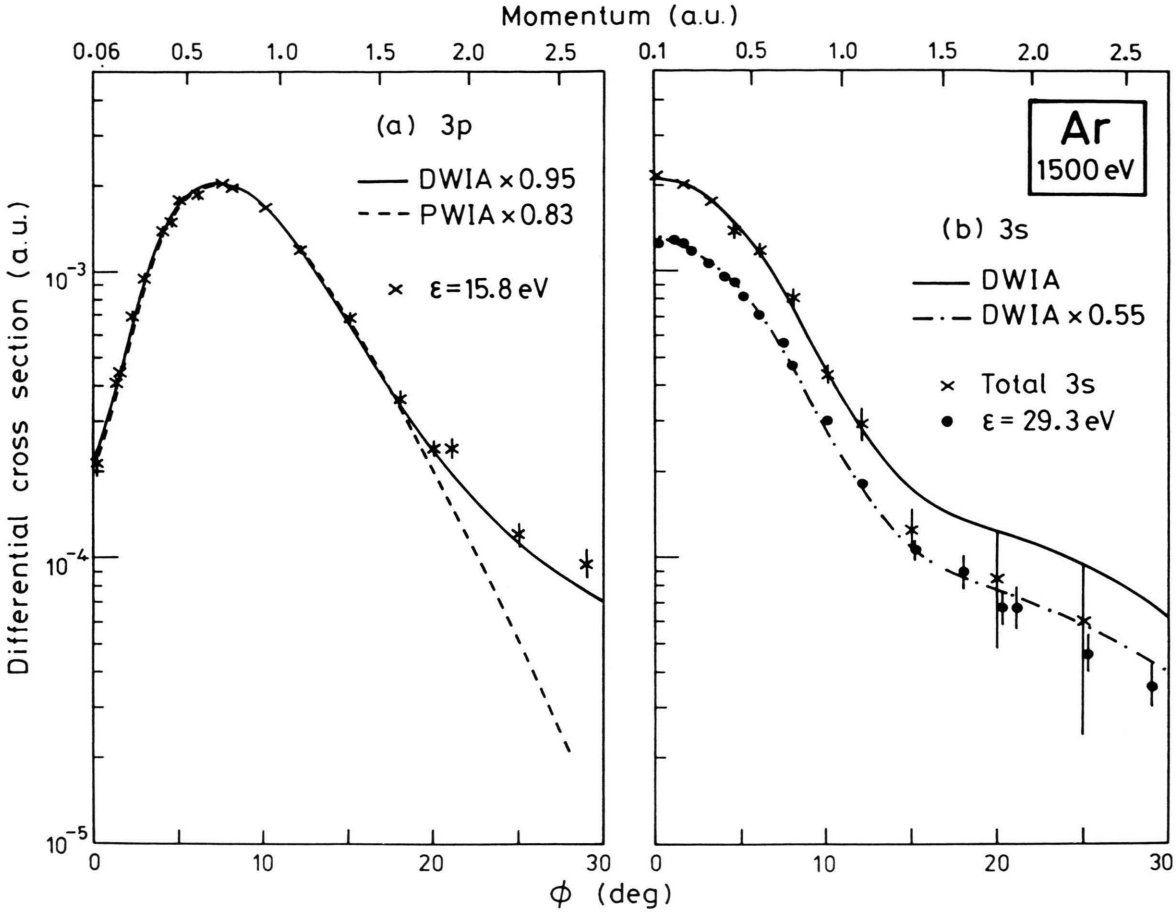

Fig. 2. The 1500 eV noncoplanar-symmetric momentum profiles for the Ar ground-state transition ($\varepsilon = 15.8$ eV), first excited state ($\varepsilon = 29.3$ eV), and the total $^2S^e$-manifold compared with the DWIA and PWIA cross-sections using (a) Hartree-Fock 3p and (b) Hartree-Fock 3s-wavefunctions.

3. EMS of Atoms

3.1. Hydrogen

The simplest application of EMS is provided by atomic hydrogen, where there is one orbital, ψ_{1s}, with separation energy $\varepsilon_{1s} = 13.6$ eV. The measurement of the hydrogen momentum profile (Fig. 1) was made by Lohmann and Weigold [7]. The measured profile is in excellent agreement with the square of the momentum-space ground-state wavefunction, $|\psi_j(q)|^2 = 8\pi^{-2}(1+q^2)^{-4}$. The fact that the momentum information is characteristic of the target and does not depend on other aspects of the collision is confirmed by the independence of the measured profile from the energies of the electrons.

3.2. Argon

The structure of argon and its ion has been a central problem in atomic structure theory for some time [4, 5]. It contains all the complications of initial-state and final-state correlations in a case where many of the final states below the double-ionisation continuum

Fig. 3. Momentum profiles for the $^2S^e$-manifold of argon and various satellites compared with calculated 3s momentum profiles multiplied by their respective spectroscopic factors [8]. The dominant configurations for the corresponding ion states and the respective separation energies are as shown. The dominant $^2S^e$-transition to the $3s3p^6$ ion state at $\varepsilon = 29.3$ eV is shown in Fig. 2b. For the $3s^2 3p^4 4s$ transition a 4s Hartree-Fock momentum profile scaled by the factor 0.0015 is also shown in Figure 3b.

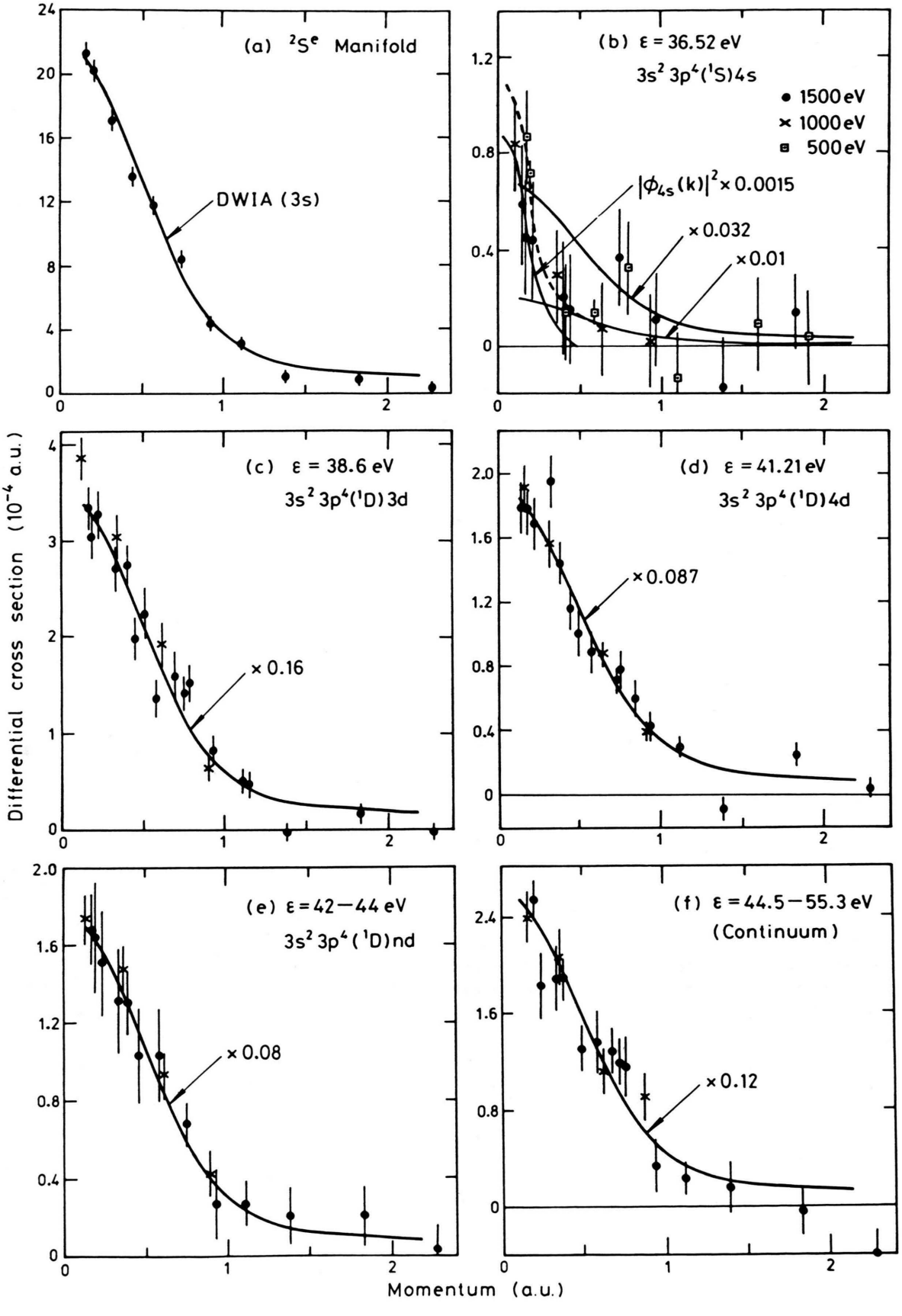
Ar $^2S^e$ MOMENTUM PROFILES
(a) $^2S^e$ Manifold
DWIA (3s)
(b) ε = 36.52 eV
$3s^2 3p^4(^1S)4s$
● 1500 eV
× 1000 eV
▫ 500 eV
$|\phi_{4s}(k)|^2 \times 0.0015$
× 0.032
× 0.01
(c) ε = 38.6 eV
$3s^2 3p^4(^1D)3d$
× 0.16
(d) ε = 41.21 eV
$3s^2 3p^4(^1D)4d$
× 0.087
(e) ε = 42 − 44 eV
$3s^2 3p^4(^1D)nd$
× 0.08
(f) ε = 44.5 − 55.3 eV
(Continuum)
× 0.12
Differential cross section (10^{-4} a.u.)
Momentum (a.u.)

Table 1. Spectroscopic factors for the $^2S^e$-manifold of argon compared with calculated values. The error in the last figure is given in parentheses.

Dominant ion-state configuration	Experiment [8]		Calculated spectroscopic factor S_f				
	ε (eV)	S_f	GF [9, 10]	GF [13]	CI [11]	FSCI [11]	FSCI [12]
$3s3p^6$	29.24	0.55(1)	0.553	0.605	0.649	0.600	0.618
$3p^44s$	36.50	0.02(1)		0.008	0.013	0.006	0.006
$3p^43d$	38.58	0.16(1)	0.199	0.135	0.161	0.142	0.112
$3p^44d$	41.21	0.08(1)	0.107	0.005	0.083	0.075	0.057
$3p^45d$	42.65	} 0.08(1)	0.042	0.025	} 0.081	} 0.095	0.021
$3p^46d$	43.40		0.021				0.009
$Ar^{++}+\varepsilon$		0.12(1)	0.076	0.177	0.013	0.08	0.18

can be experimentally resolved. In addition, there are two occupied valence states, 3p and 3s, in the target Hartree-Fock configuration of the ground state, so that it is possible to test the consistency of the spectroscopic-factor determination in EMS.

The outer-valence 3 p-manifold is dominated by the transition to the ground state of the ion. McCarthy et al. [8] measured the spectroscopic factor for this transition to be 0.95 ± 0.02. Its momentum profile at 1500 eV is described within experimental error by the Hartree-Fock 3p momentum distribution and the distorted-wave impulse approximation (DWIA), which allows for distortion of the continuum electrons in the probe factor (Eq. (6)) owing to elastic scattering by local central potentials representing the spectator particles [4]. It is also well described up to $q \sim 1.7$ a.u. by the PWIA using the Hartree-Fock 3p-wavefunction to describe the struck electron (see Figure 2). In the high-momentum region, above $q \sim 1.7$ a.u., the PWIA underestimates the cross-section, the log plot accentuating this difference. In the high-momentum region of the wavefunction, which is dominated by the inner region of the corresponding position-space wavefunction, i.e. the region close to the nucleus, distortion effects should become more important. McCarthy et al. [8] normalised their measured cross-sections at $\phi = 10°$ to the $3p^{-1}$ DWIA cross-section for the ground-state transition obtained by multiplying the calculated $3p^{-1}$-manifold cross-section by the ion ground-state spectroscopic factor of 0.95 (Eqs. (12) and (13)).

The 3s-manifold, on the other hand, has a large number of states with significant spectroscopic strength, the separation energy spectra showing rich structure extending from the lowest-energy 3s hole state at 29.24 eV to well above the double-ionisation threshold at 43.6 eV [4, 5, 8]. The shapes of the different momentum profiles for the strongly-excited states at large separation energy, and also that of the continuum above the double-ionisation threshold, are independent of energy and have the characteristic shape of 3s Hartree-Fock momentum distributions up to over 1 a.u. of momentum. Figure 2b shows that the DWIA with the target Hartree-Fock 3s momentum distribution describes the shape and normalisation of the whole $^2S^e$-manifold structure factor for all momenta (or ϕ). The cross-section for the transition at 29.24 eV, with dominant ion configuration $3s\,3p^6(^2S^e)$, is also well described by the DWIA plus target Hartree-Fock approximation using a spectroscopic factor of 0.55. The momentum profiles for other $^2S^e$ final states, as well as contributions in the continuum, are also accurately described by the calculated 3s-profile (Figure 3), the only exception being the 36.52 eV transition to the state with dominant $3s^2\,3p^4(^1S)4s$ configuration. This shows the possibility of a 4s configuration-interaction (CI) component in the Ar ground state at the 0.15% level. The spectroscopic factors for the $^2S^e$-manifold are independent of energy in the range 500–1500 eV and of momentum in the range 0–2 a.u. They are listed in Table 1 together with some calculated spectroscopic factors.

The final-state configuration-interaction (FSCI) calculations listed in Table 1 include only final-state correlation, whereas the CI and the Green's function (GF) calculations include initial-state correlations and relaxation as well as final-state correlations. None of the calculations adequately describes the data, although those of Amusia and Kheifets [9, 10] obtain the correct spectroscopic factor for the main transition.

Since initial-state correlations play a very small rôle in the $^2S^e$-manifold, the energy of the 3s-orbital may be obtained using the weighted mean of final states belonging to the $^2S^e$-manifold, (15). The result is

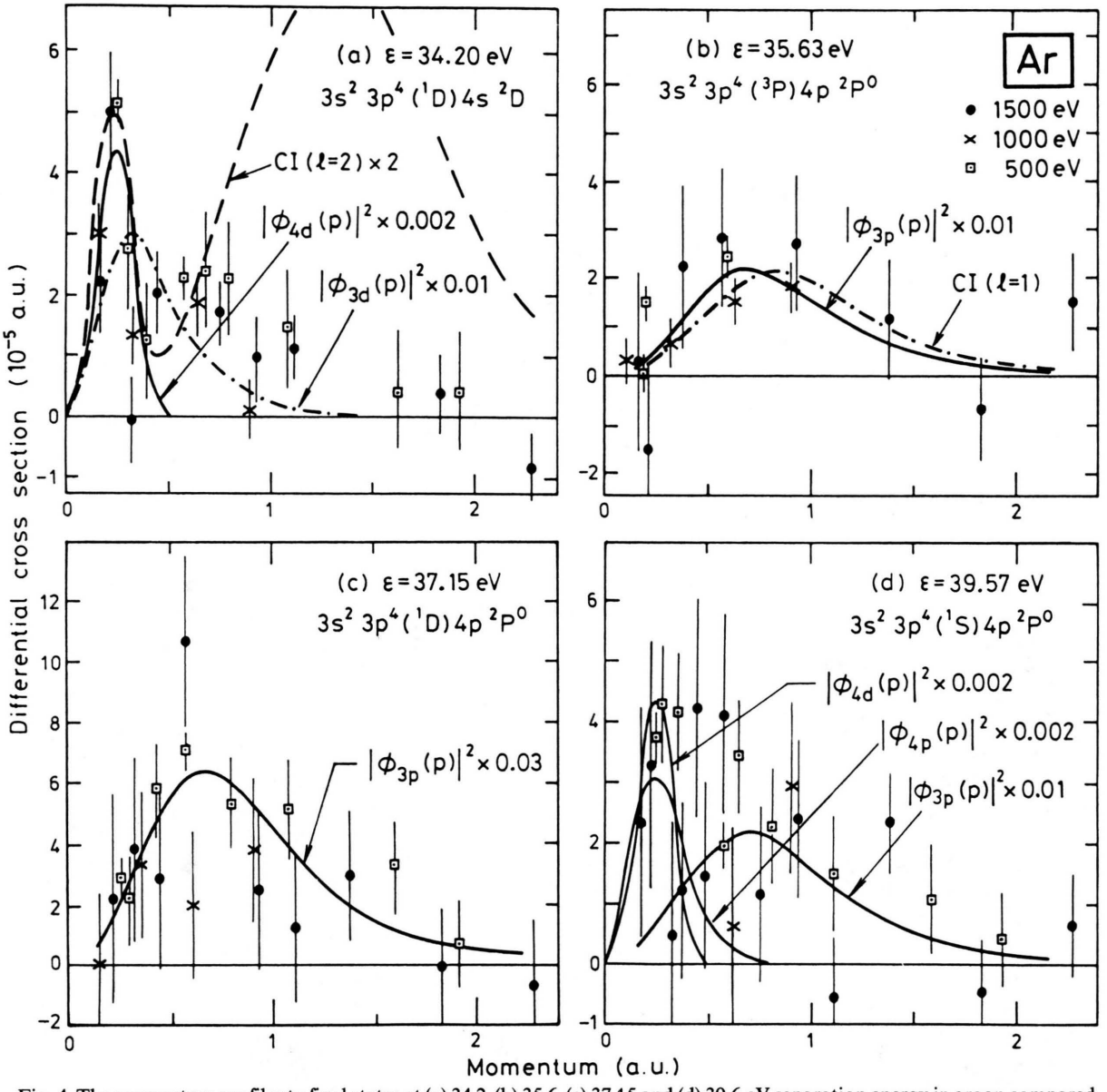

Fig. 4. The momentum profiles to final states at (a) 34.2, (b) 35.6, (c) 37.15 and (d) 39.6 eV separation energy in argon compared with several calculated distributions [8]. The curves labelled CI are the full-overlap calculations [11] multiplied by appropriate factors. The other curves are Hartree-Fock orbital momentum distributions weighted by the indicated spectroscopic factors.

$\varepsilon_{3s} = 35.2 \pm 0.2$ eV, which compares very well with the Hartree-Fock value of 34.76 eV.

Although the dominant features in the argon separation-energy spectra above the $^2P^0$ $3s^2 3p^5$ ion ground state at 15.76 eV and the $^2S^e$ $3s 3p^6$ ion excited state at 29.3 eV are due to transitions to states belonging to the $^2S^e$-manifold, weak transitions belonging to both the $^2D^e$ and $^2P^e$-manifolds have been identified [8]. The $^2D^e$-transitions can only occur if there are d-wave correlations in the Ar ground state. The most prominent $^2D^e$-transition is to the $3s^2 3p^4(^1D)4s$ state at 34.20 eV, and its momentum profile, shown in Fig. 4a, is very interesting. It has a narrow peak at $q \sim 0.25$ a.u., which is to be expected from the diffuse (in coordinate space) spectroscopic 3d and 4d-orbitals. The Hartree-Fock 3d and 4d momentum distributions are shown

in Fig. 4a multiplied by the normalisation factors indicated, which must be smaller than or equal to the square of the corresponding CI expansion coefficient for the d-wave configurations in the argon ground state. The low-momentum region is best described by the 4d wavefunction. If the intensity of the low-momentum peak is attributed to, say, a ground-state $3s^2 3p^4(^1D)4s\,4d$ configuration it would require only a 0.4% admixture of this configuration in the argon ground state to account for its intensity.

Mitroy et al. [11] carried out a full calculation of the overlap function between the correlated Ar ground state and correlated final states. The $^2D^e$-manifold momentum distribution calculated by Mitroy et al. is shown in Fig. 4a, multiplied by a factor of 2. Clearly this calculation underestimates the intensity of the small-momentum peak and overestimates the contributions at high momentum. Mitroy et al. found that the dominant contribution of the correlation energy came from "correlating" pseudo-natural orbitals rather than the spectroscopic (Hartree-Fock) orbitals. These pseudo-orbitals are localised in the same region of space as the spectroscopic 3s and 3p-orbitals and therefore give rise to momentum contributions at much higher momenta than those given by the diffuse spectroscopic 3 d and 4 d-orbitals. The measurements show that the spectroscopic 4d-orbital is more important than given by the calculation of Mitroy et al., who overestimate the large-momentum components due to the 3d pseudo-orbital.

The transition at $\varepsilon = 39.6$ eV also has a very similar momentum distribution to that for the $3s^2 3p^4(^1D)4s$ $^2D^e$ state (Figure 4d). This could be due to excitation of the $3s^2 3p^4(^3P)4d$ $^2D^e$ ion state at 39.64 eV. Some of the cross-section is also probably due to the excitation of the $3s^2 3p^4(^1S)4p$ $^2P^0$ ion state at 39.57 eV. McCarthy et al. also find two definite $^2P^0$-transitions (Figs. 4b and 4c) with spectroscopic factors of 0.01 and 0.03, respectively, in addition to the dominant ground-state transition. Both transitions show the 3p momentum distribution.

3.3. Xenon

The importance of relativistic effects on the outer valence orbitals of atoms was first demonstrated by Cook et al. [14]. Their 1200 eV EMS measurements showed that the $5p_{3/2}$ and $5p_{1/2}$ electron momentum distributions differed significantly from each other and could not be described by non-relativistic wavefunctions, but that they were in excellent agreement with those given by relativistic Dirac-Fock wavefunctions (Figure 5). Although both the $5p_{3/2}$ and $5p_{1/2}$ momentum densities peak around 0.5 a.u., electrons in the $5p_{3/2}$-state have considerably higher probability of having low momentum than do the $5p_{1/2}$-electrons.

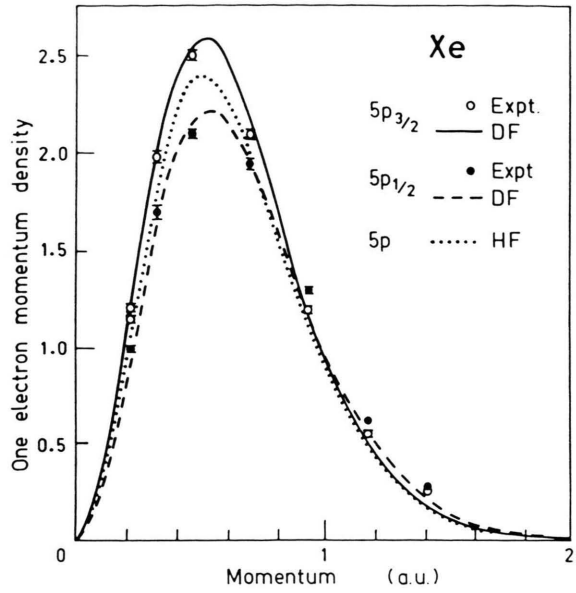

Fig. 5. The one-electron momentum densities for the $5p_{3/2,\,1/2}$-orbitals in xenon compared with Dirac-Fock (solid and dashed lines) and Hartree-Fock (dotted line) wavefunctions [14].

3.4. Lead

Lead not only shows strong relativistic effects in the observed momentum profiles, but it also shows significant correlation effects in both initial and final states [15]. It provides a stringent test of the configuration-interaction Dirac-Fock method.

In the independent-particle model, the valence orbitals of lead are $(6s)^2\,(6p)^2$. In *jj*-coupling the two 6p-electrons would be in the $6p_{1/2}$-state, whereas in *LS*-coupling the $6p_{1/2}:6p_{3/2}$ branching ratio would be 0.5. The observed momentum-dependent branching ratio is compared with the result of multi-configuration Dirac-Fock (MCDF) extended-average-level (EAL) and optimal-level (OL) initial ground-state calculations in Fig. 6, as well as with a full-CI overlap-amplitude calculation using MCDF-OL wavefunctions for both the initial as well as final states [15]. Although the observed branching ratio is mainly due

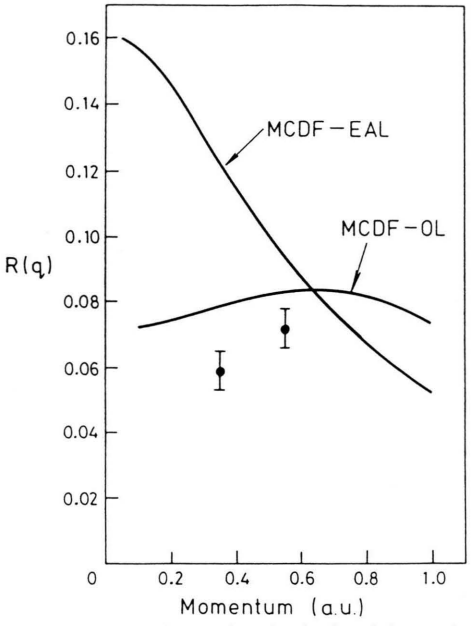

Fig. 6. The experimental and calculated $6p_{3/2}:6p_{1/2}$ branching ratios for lead, plotted as a function of the momentum q [15].

to initial correlations, final-state correlations do play a small, but significant rôle.

The momentum distributions for the 6p and 6s-transitions are well described by the relativistic orbital wavefunctions, but much less well by the nonrelativistic Hartree-Fock orbitals (Figure 7). Excellent agreement is obtained between the calculated and measured spectroscopic factors for the 6s-transitions as well as the 6 p ones [15], the 6s-splitting being, however, due mainly to final-state correlation.

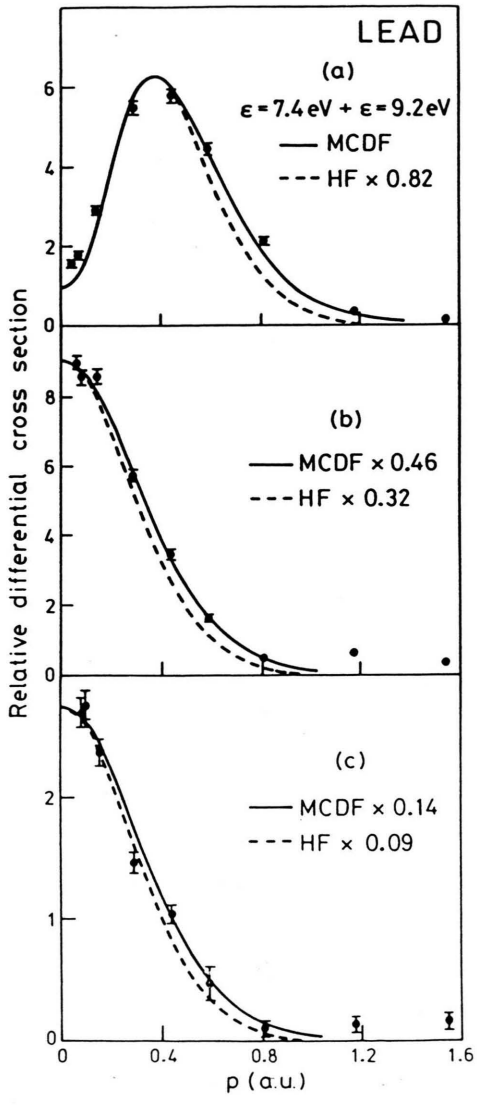

Fig. 7. EMS momentum profiles for lead at 1000 eV compared with relativistic and Hartree-Fock wavefunctions for (a) the 6p-manifold and the two main 6s-transitions at $\varepsilon = 14.6$ eV (b) and 18.4 eV (c).

4. Electron Momentum Spectroscopy of Laser-Excited Atoms

Excited target atoms can be prepared in well-defined states by optically pumping atoms with a tuneable laser. By using polarised laser light it is possible to excite specific magnetic substates. This offers the possibility of measuring momentum distributions for excited targets as well as for atoms in aligned and oriented states. In the recent measurements of Zheng et al. [16] and Bell et al. [17], sodium atoms are optically pumped by right-hand circularly-polarised laser light tuned to the $3^2S_{1/2}(F=2) \leftrightarrow 3^2P_{3/2}(F'=3)$ transition.

The experimental arrangement is shown in Figure 8. A detailed description of the multiparameter-coincidence spectrometer and the associated circuitry is given in [18]. The sodium oven is mounted out of the plane of Fig. 8 and produces a sodium beam perpendicular to, and intersecting, the horizontal laser beam and vertical electron beam, thus defining the interaction region. In order to obtain the highest fraction of the population in the $3^2P_{3/2}$ ($F'=3$) excited state, the Doppler broadening of the sodium beam has to be

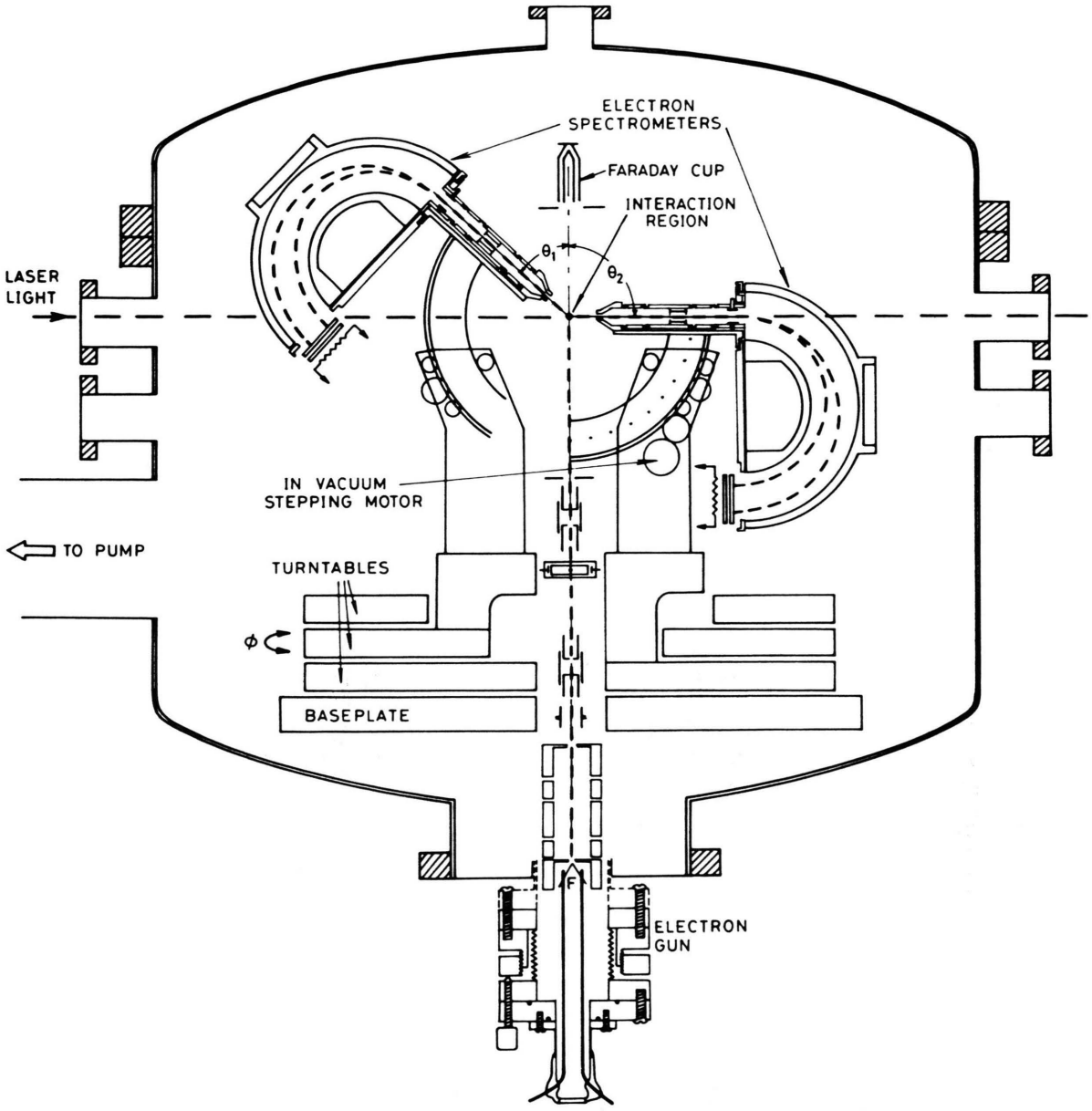

Fig. 8. Schematic view of the multiparameter (e, 2e) coincidence spectrometer. The electron beam, laser beam, and sodium beam intersect at right angles. The sodium oven (not shown) is mounted perpendicular to the plane of the diagram. In the measurements, $\theta_1 = \theta_2 = 45°$ and ϕ is varied. The hemispherical energy analysers are preceded by a five-element retarding and focusing lens. The position-sensitive detector at the exit aperture of the analyser determines the arrival time and the energy of each detected electron.

limited to about 20 MHz. This means that the sodium beam has to be well collimated with a maximum divergence of about 1°. The sodium beam is trapped by a refrigerated finger in order to keep the electron spectrometers clean and to maintain high-vacuum conditions.

The optical arrangement used is shown in Fig. 9. An argon ion laser pumps a tunable CW ring dye laser whose light is then right-hand circularly polarised using a linear polariser and quarter-wave plate. A split photodiode is used to keep the laser tuned to the $3^2S_{1/2}(F=2) \leftrightarrow 3^2P_{3/2}(F'=3)$ transition for atoms in

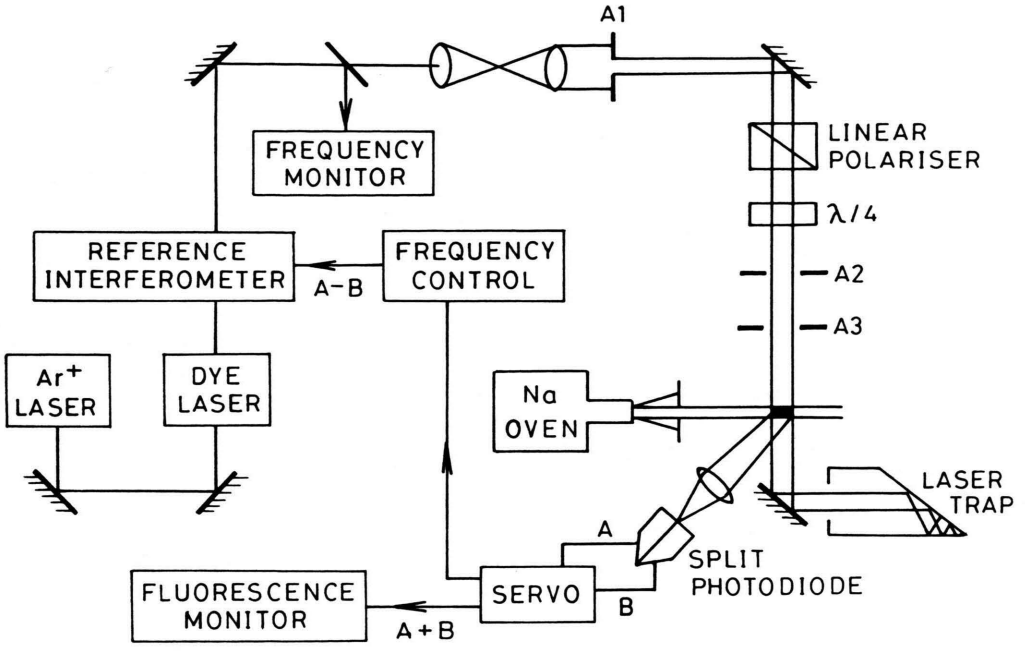

Fig. 9. The arrangement of the optical system for laser excitation of sodium atoms. For details see text.

the narrow sodium beam. The fluorescence from the decay of the $3^2P_{3/2}(F'=3)$ state back to the $3^2S_{1/2}$ $(F=2)$ ground state is imaged with a simple lens onto the split photodiode. Owing to the small but finite divergence of the sodium beam, the atoms in that part of the atomic beam moving towards the laser beam absorb light at a slightly lower frequency than those travelling away from ther laser beam. Thus the brightest portion of the fluorescence spot is seen to move if the frequency of the laser drifts slightly. When the spot moves, one half of the split photodiode receives more signal than the other, and vice versa. The difference between the two photodiode signals is then used as an error signal in a feedback loop that controls the frequency of the dye laser. The sum signal of the split photodiode provides information on the intensity of the laser and the density of the atomic beam.

In the stationary condition, pumping with σ^+-light produces a population of the $F=2$, $m_F=2$ ground state with about 12% of the beam in the $F'=3$, $m_{F'}=3$ excited state. This means that in the excited state there is no population in the $m_l=0$ (i.e. $3p_z$) orbital, all being in the $m_l=+1$ state, corresponding to 50% in both the $3p_x$ and $3p_y$-orbital. The momentum densities for the three degenerate orbitals are shown schematically in Fig. 10, the $3p_z$-orbital being unoccupied.

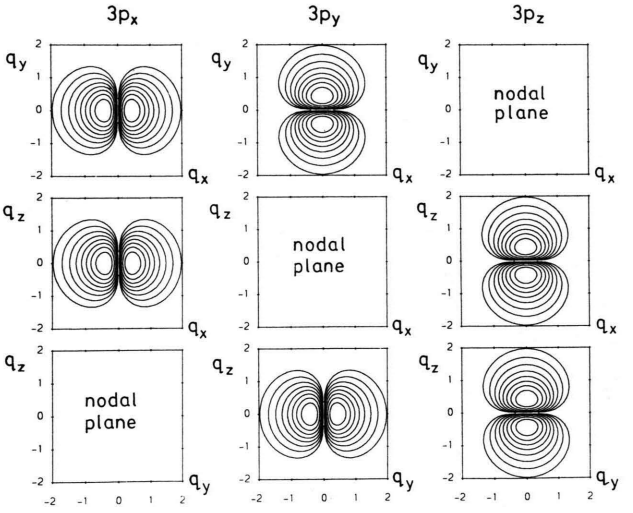

Fig. 10. Schematic momentum-density contour maps of the three degenerate 3p-orbitals of sodium. The measurement probes the momentum density of the $3p_y$-orbitals along the q_x-axis, the $3p_z$-orbital being unoccupied.

The axis of quantisation, z, has been chosen as the direction of propagation of the circularly-polarised pumping beam, the atomic sodium beam is incident in the x-direction, and the electron beam is incident in the y-direction. This is shown schematically in Fig. 11,

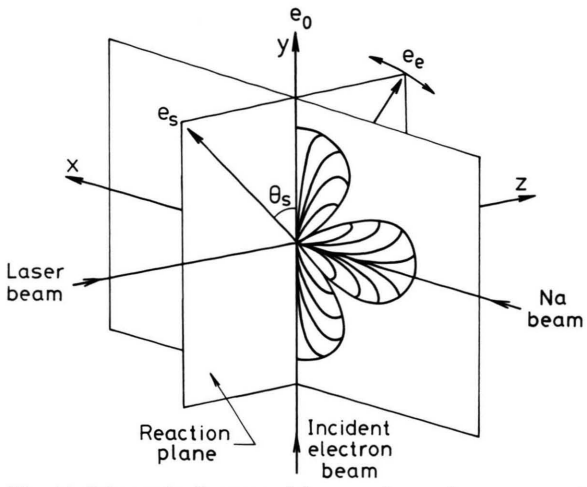

Fig. 11. Schematic diagram of the experimental arrangement and the electron charge and momentum densities of the excited 3p ($m_l=1$) sodium atoms. The momentum is probed along the x-direction with $q_y \sim q_z \sim 0$.

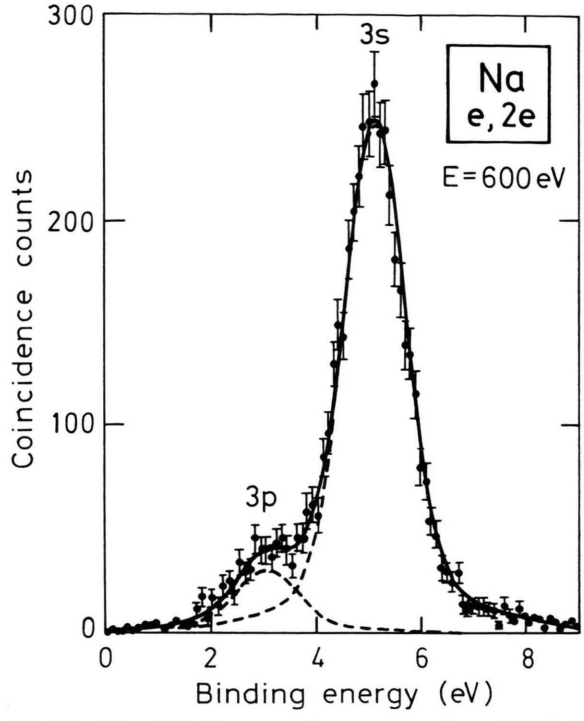

Fig. 12. The 600 eV noncoplanar-symmetric separation-energy spectrum at $\phi = 2.5°$ for sodium with laser on.

which also shows schematically the $3p_z$ and $3p_y$-distribution of the charge cloud of the sodium in the 3p ($m_l=+1$) excited state. The scattering plane is the zy-plane, and both outgoing electrons make a polar angle of 45° with respect to the incident (y) direction, the out-of-plane azimuthal angle of one electron is varied to probe the different momentum components of the target. Thus the experiment measures the (e, 2e) triple-differential cross-section as a function of the x-component of momentum, q_x. For the symmetric noncoplanar kinematics employed, $E_e = E_s$ and $\theta_e = \theta_s = 45°$, the z and y-components of momenta are fixed and essentially zero for small binding energies. The experiment therefore measures the momentum density of the $3p_x$-orbital along the $q_y = q_z = 0$ axis (Figure 10).

Figure 12 shows the separation-energy spectrum obtained for sodium at $\phi = 2.5°$ with the laser on. Ionisation from atoms in the excited $^2P_{3/2}$-state can be seen quite clearly. The momentum distributions obtained for the 3s ground-state transition and for the 3p ($m_l=1$) excited state are shown in Figs. 13a and b, respectively, compared with calculated momentum distributions given by the Hartree-Fock 3s and 3p ($m_l=+1$) wavefunctions. The finite angular (i.e. momentum) resolution has been included in the calculations. The main effect of the finite angular resolution is to fill in the $3p_x$ momentum distribution at momenta close to zero. The momentum distribution for the excited state peaks at very small momenta (~0.2 a.u.) because of the diffuse nature of the 3p-orbital in coordinate space. Also shown in the figure for comparison is the momentum distribution expected for the $m_l=0$ substate of the 3p-state. That for the unoriented $3p_{(0,\pm1)}$-state is similar to that for the $m_l=1$ substate, but is in significantly poorer agreement with the data owing to the inclusion of the $m_l=0$ component. The momentum distribution for the $m_l=0$ (i.e. $3p_z$) state is, of course, zero along the q_z axis ($q_y=q_z=0$), since the $3p_z$ (dumbbell) orbital is perpendicular to the nodal xy-plane, the node being at the origin. However, owing to the finite momentum resolution, there is a small probability of seeing some $m_l=0$ contribution if there were any atoms in this excited magnetic substate, this probability decreasing as one moves away from the origin along the q_z (or for that matter the q_y) direction. This explains the "anomalous" shape of the calculated $m_l=0$ ($3p_z$) momentum distribution along the q_x-axis.

The study of laser-excited targets opens exciting new avenues. It makes it possible to study oriented and aligned targets, and to examine how the remainder of the electron cloud adjusts to one of the electrons being in an excited state. At high laser intensities it

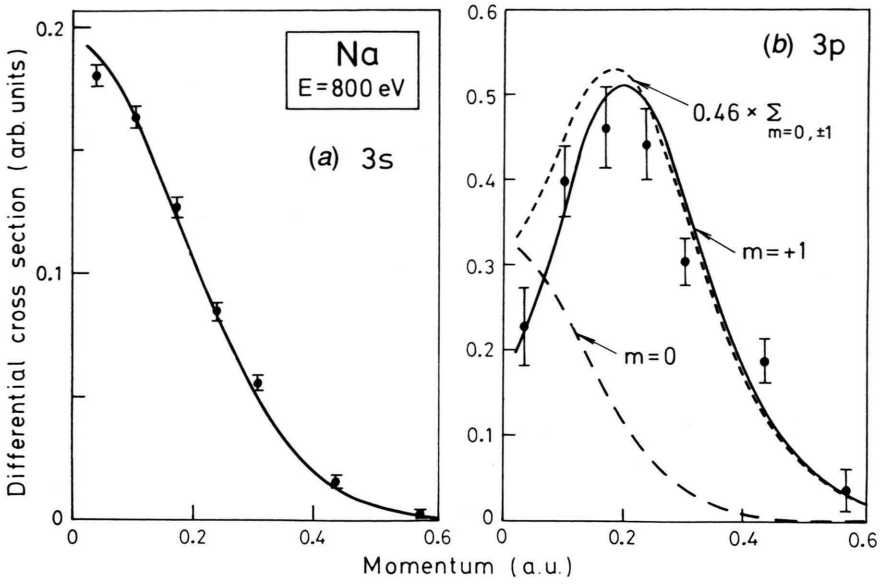

Fig. 13. The momentum distributions for (a) the 3s ground state and (b) the 3p ($m_l=1$) excited state of Na compared with Hartree-Fock momentum distributions.

should also be possible to do measurements on "dressed" targets (see for example [19]).

5. Molecules

The EMS study of molecules began with the measurement of the momentum profiles of the valence orbitals of methane by Hood et al. [20] and of hydrogen by Weigold et al. [21]. Since then an extremely fruitful collaborative effort has evolved between theoretical quantum chemistry and experimental EMS. In particular this collaboration has led to the development of very accurate Hartree-Fock-limit and correlated wavefunctions for H_2O [22].

The measured momentum distributions for the outer valence orbitals of H_2O are shown in Fig. 14, together with calculated momentum distributions given by several MO calculations as well as two complete CI overlap calculations (Eq. (10)). The calculations have been normalised to the measured $1b_2$ momentum profile. The very precise SCF calculations of Bawagan et al. [22] effectively converge at the Hartree-Fock limit for total energy, dipole moment and momentum distribution. The observed significant discrepancies in calculated SCF and measured momentum distributions are independent of the basis set. They were, however, largely removed by CI calculations of the full target–ion overlap amplitude. The CI wavefunctions for the final ion and target ground states, generated from the accurate Hartree-Fock limit MO basis sets, accounted for up to 88% of the correlation energy. This work clearly shows the need for an adequate consideration of electron correlation in describing the low-momentum parts of the $1b_1$ and $3a_1$ electron distributions. It also shows the need for including diffuse functions in the basis sets [27].

Similar disagreement between the EMS momentum profiles and Hartree-Fock-limit orbital momentum distributions is evident in the outermost orbitals of the other second-row hydrides HF [28] and NH_3 [29], the EMS measurements consistently showing more momentum density at low momentum. The inclusion of correlation effects leads to much better agreement with the data.

In contrast to the second-row hydrides, the measured orbital momentum distributions for the third-row hydrides H_2S [30], PH_3 [31] and SiH_4 [32] are in excellent agreement with Hartree-Fock orbital wavefunctions. The addition of correlation and relaxation to the wavefunctions (i.e. calculating the full overlap) produces little or no change from the momentum distributions predicted using Hartree-Fock-limit wavefunctions with saturated basis sets.

Some recent data for ethyne [33] are shown in Figure 15. Here again there is excellent agreement between theory and experiment for both the shapes as well as the relative magnitudes of the valence-orbital

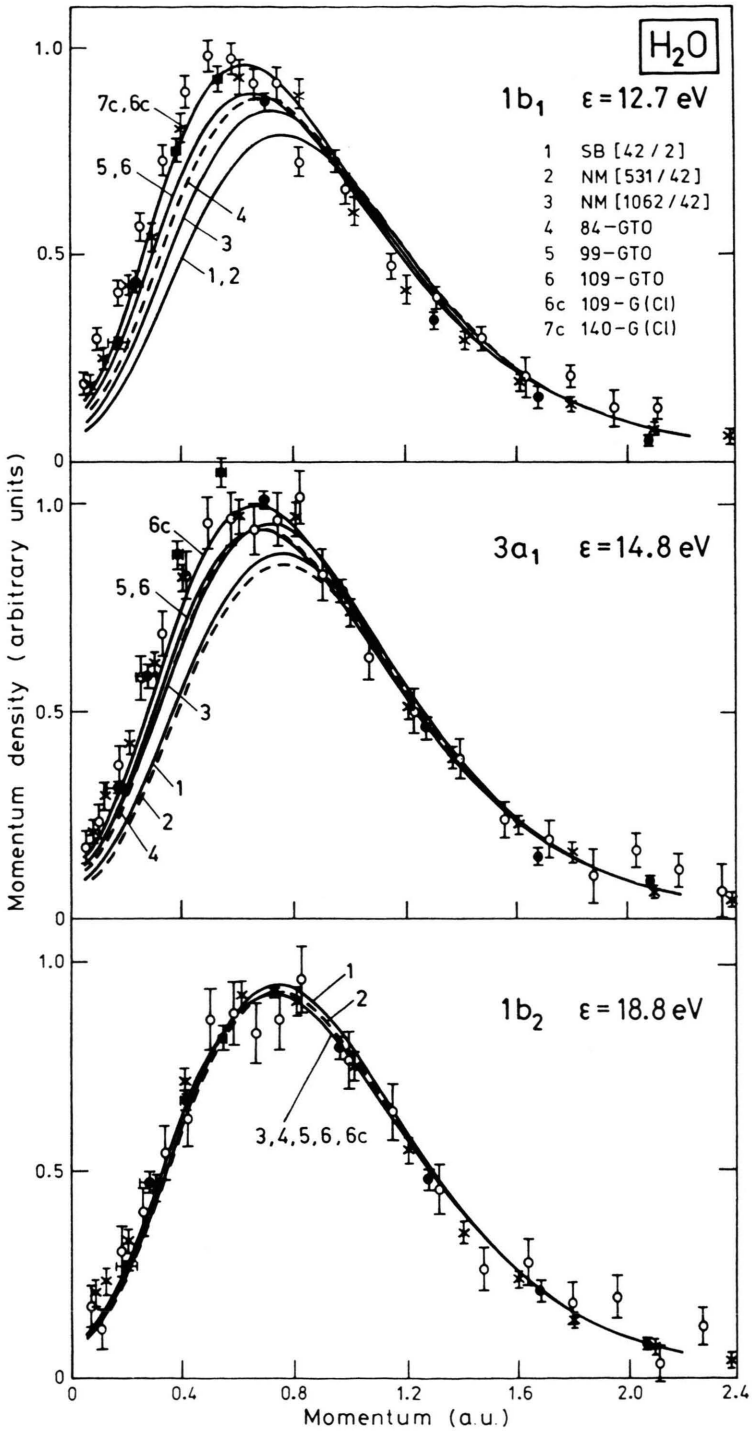

Fig. 14. Comparison of the experimental momentum distributions of the outer-valence $1b_1$, $3a_1$, and $1b_2$-orbitals of H_2O with spherically averaged momentum distributions calculated using (a) molecular-orbital wavefunctions 1 [23]; 2, 3 [24]; 4–6 extended GTO basis sets [22]; (b) (6c) and (7c) the full overlap amplitude calculated with CI wavefunctions generated by 109 and 140 GTO basis-function sets for the initial ground state and final ion states [22]. The open circles are the 1200 eV data of [22] and the full circles that of [25]; the crosses are 1800 eV data [26].

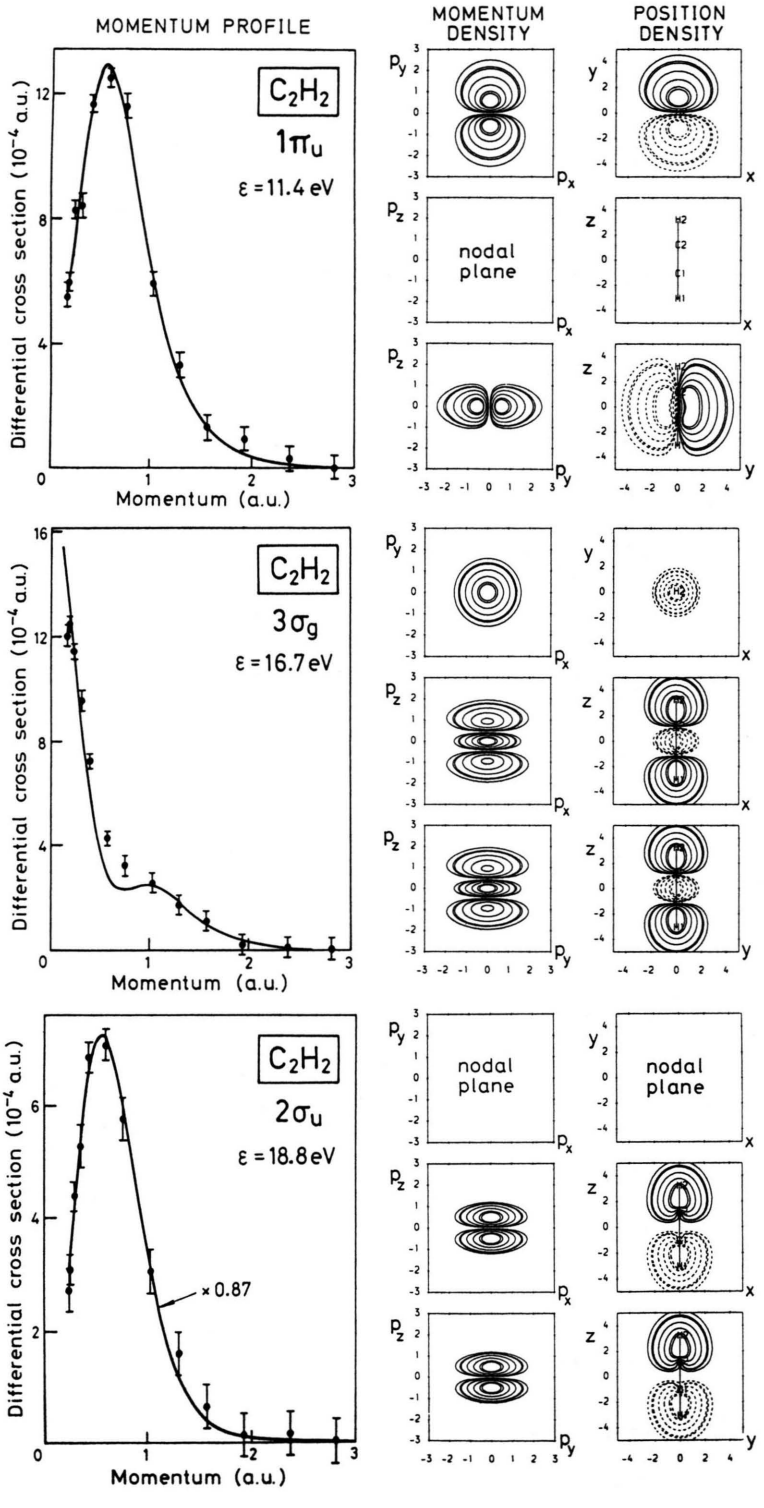

Fig. 15. Measured and calculated spherically-averaged momentum densities for the outer-valence orbitals of ethyne together with the calculated density contour maps [33].

momentum densities. The present theoretical models of the electronic structure of C_2H_2 are quite adequate, in contrast to the conclusions reached in earlier studies (see [33]).

6. The Spectral Momentum Density of Amorphous Carbon

The (e, 2e) technique can be used to obtain the spectral momentum density of electrons in solids, that is the probability of an electron possessing a particular value of binding energy ε and momentum $\boldsymbol{q}$ (16). Ritter, Dennison, and Jones [34] reported the first spectral momentum density measurement of the valence band of a solid, the target material being an amorphous carbon film. With an (e, 2e) energy resolution of approximately 6 eV, they were barely able to resolve two bands in the binding-energy spectrum.

There has been considerable interest in determining the electronic properties of amorphous carbon (see [35] and references therein). Amorphous carbon (a-C) films range from black, soft, "graphitic" films to hard, transparent, "diamond-like" films depending on the method of preparation and the concentration of hydrogen in the sample [34]. The structure of a-C films is still not understood.

In order to obtain further information on the electronic structure of a-C, we have undertaken a series of (e, 2e) measurements on evaporated films of a-C at much higher energy resolution than the earlier work. In the present work a primary electron beam of 10 keV plus binding energy intersects a free-standing 80 Å amorphous carbon film. Scattered electrons leaving the collision region at angles of 45° with respect to the incident-beam direction pass through two identical hemispherical electrostatic analysers positioned on opposite sides of the beam. The analysers are used to determine the momenta and arrival times of each emitted electron by means of position-sensitive detectors [36]. Each analyser is adjusted to accept electrons in a 20 eV band of energies centred around 5000 eV. The combined energy resolution of each analyser and detector together is about 1 eV. Different values of momenta $\boldsymbol{q}$, perpendicular to the incident direction and in the scattering plane, are sampled by varying $\Delta E = E_s - E_e$ and keeping $E_s + E_e = E_0 - \varepsilon(\boldsymbol{q})$ constant. The values of q are given by [37]

$$q = k_0 \frac{\Delta E}{2E_0}\left(1 + \frac{\varepsilon}{E_0}\right). \tag{17}$$

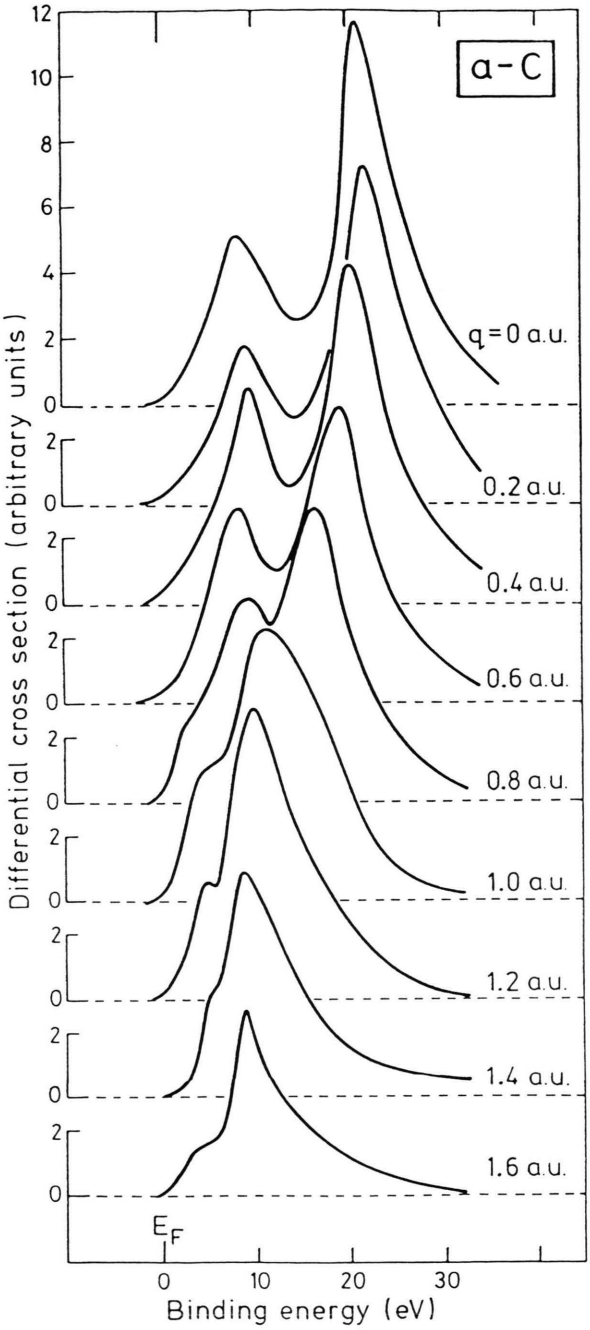

Fig. 16. Spectral momentum density measurements for amorphous carbon [37, 38].

Figure 16 shows binding-energy spectra obtained at different target-electron momenta [38]. This is a plot of the spectral momentum density. The low-energy peak is attributed to the excitation of a graphitic π-band and the higher-energy peak to the excitation of gra-

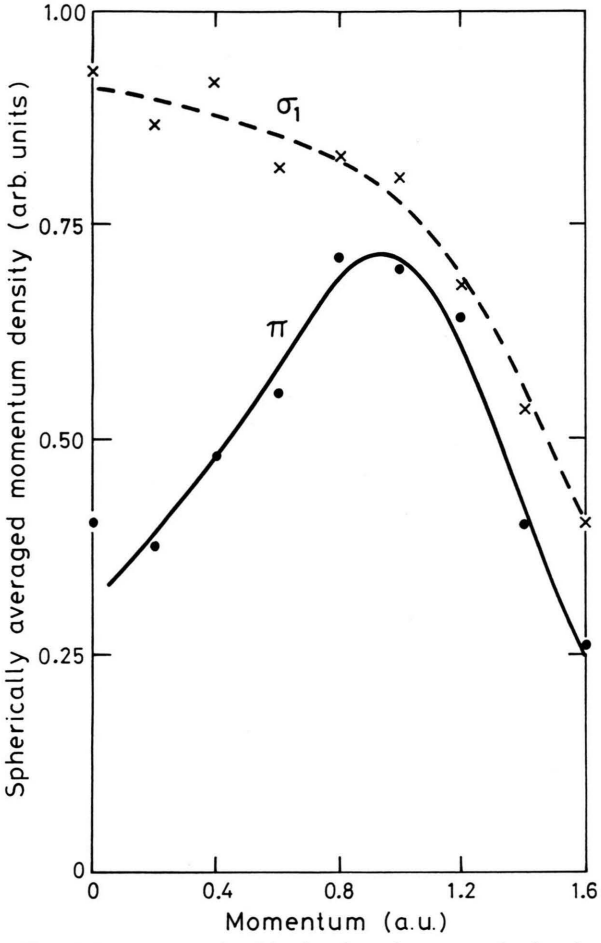

Fig. 17. Momentum densities for the valence π and σ-bands of amorphous carbon [37, 38].

phitic σ-bands. The data have been deconvoluted to allow for the effects of energy loss by incident and scattered electrons within the target material due to multiple scattering. The strongly dispersive nature of the higher-energy σ-band can be seen from the figure. The outer π-band also shows some dispersion. In addition to the dispersion, there is for both bands a marked change in intensity as a function of q. This is displayed in Fig. 17, which shows the momentum density as a function of q for the two bands.

The band structure of graphite as calculated by Gao et al. [35] is shown in Fig. 18, and the momentum densities for the π and three σ-bands in Figure 19. The lowest σ-band is σ_1 and its wavefunction is s-like, i.e. the momentum density is maximum at $q=0$ and decreases monotonically as q increases. The wavefunctions for the upper two σ-bands are p-like, the momen-

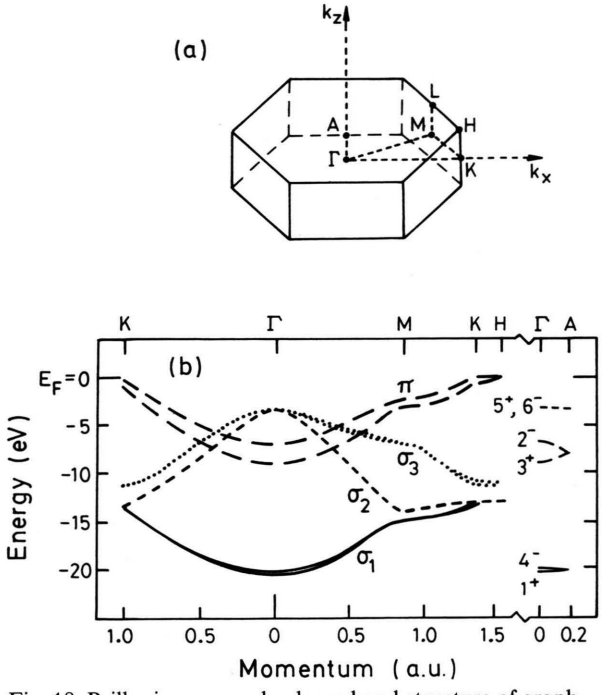

Fig. 18. Brillouin zone and valence band structure of graphite [35].

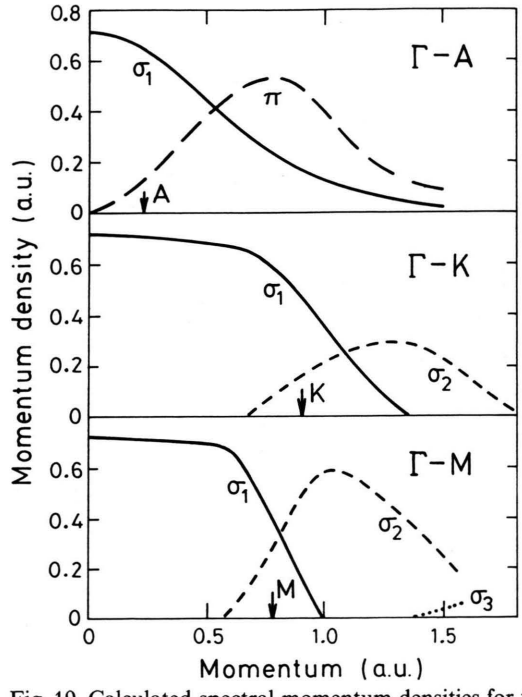

Fig. 19. Calculated spectral momentum densities for the valence bands of graphite in the different crystal directions [35].

tum density being zero at $q = 0$, and rising abruptly from zero near the Brillouin-zone boundary to peak in the second and third zones, and then falling as q increases. Thus the σ_2 and σ_3-bands are essentially unoccupied at small $\boldsymbol{q}$ (≤ 0.5 a.u.). The momentum density for the π-band is zero for $\boldsymbol{q}$ in the $\Gamma-K-M$ plane, since the π-orbital has a node there. For $\boldsymbol{q}$ along the c-axis perpendicular to the basal plane, the momentum density of the π-band displays p-wave character, it is zero at the origin and peaks at $q \approx 0.7$ a.u. In the present work we expect random orientations in the disordered phase of the evaporated films. This would still preserve the p-wave and s-wave character of the π and σ_1-bands, respectively.

Figure 17 shows that the σ_1-band does indeed have s-wave character, having the greatest momentum density at smaller $\boldsymbol{q}$. The momentum density for the lower-energy π-band does increase somewhat with q, as expected from the predicted p-wave character. There is some evidence that for diamond-like structures the momentum density for the outer-valence band does not go to zero [35]. The spectral density for the π-band is rather larger than expected for graphite. The data are therefore not consistent with the film being purely graphitic.

7. Summary

The power of (e, 2e) reactions under EMS kinematic conditions to provide sensitive information on the electronic structure of atoms and molecules has by now been amply demonstrated. In many cases the Hartree-Fock or Dirac-Fock picture provides a good description of the target and ion. In many other cases, particularly in the inner-valence shells, electron correlation effects dominate the structure. These can be probed accurately with EMS, and their origin pinpointed. In partnership with quantum-chemical calculations, EMS has provided a powerful tool for elucidating the structure of atoms and molecules.

The application of lasers to excite and align or orient targets has given rise to a new line of research. It is now possible to study short-lived species as well as to study the momentum densities of gaseous targets that have been aligned and/or oriented in space.

The work on solids is still in its infancy. However, the early results on amorphous carbon clearly indicate its potential for elucidating the electronic structure of condensed-matter targets.

Acknowledgements

I am grateful to the Australian Research Council for providing support of this work. I would also like to acknowledge the essential contributions played by the other members of the Flinders (e, 2e) group.

[1] E. Weigold, in: Electronic and Atomic Collisions (D. C. Lorents, W. E. Meyerhoff, and J. R. Peterson, eds.), Elsevier B. V. 1986, p. 125.
[2] J. Lower and E. Weigold, J. Phys. B **23,** 2819 (1990).
[3] E. Weigold, in: Electronic and Atomic Collisions (W. R. MacGillivray et al., eds.), IOP Publ., 1992, p. 231.
[4] I. E. McCarthy and E. Weigold, Rep. Prog. Phys. **51,** 299 (1988); **54,** 789 (1991).
[5] I. E. McCarthy and E. Weigold, Phys. Rep. C **27,** 275 (1976).
[6] S. Dey, I. E. McCarthy, P. J. O. Teubner, and E. Weigold, Phys. Rev. Lett. **34,** 782 (1975).
[7] B. Lohmann and E. Weigold, Phys. Lett. **86A,** 139 (1981).
[8] I. E. McCarthy, R. Pascual, P. Storer, and E. Weigold, Phys. Rev. A **40,** 3041 (1989).
[9] M. Amusia and A. S. Kheifets, J. Phys. B **18,** L679 (1985).
[10] A. S. Kheifets, in: Correlations and Polarization in Electronic and Atomic Collisions and (e, 2e) Reactions (P. J. O. Teubner and E. Weigold, eds.), IOP Publ., 1992, p. 187.
[11] J. D. Mitroy, K. Amos, and I. Morrison, J. Phys. B **17,** 1659 (1984).
[12] A. Hibbert and J. E. Hansen, J. Phys. B **20,** L245 (1987).
[13] W. von Niessen (1987), personal communication.
[14] J. P. D. Cook, J. Mitroy, and E. Weigold, Phys. Rev. Lett. **52,** 1116 (1984).
[15] L. Frost, J. Mitroy, and E. Weigold, J. Phys. B **19,** 4063 (1986).
[16] Y. Zheng, I. E. McCarthy, E. Weigold, and D. Zhang, Phys. Rev. Lett. **64,** 1358 (1990).
[17] S. Bell, Y. Shen, E. Weigold, and Y. Zheng, Proc. 17th ICPEAC (I. E. McCarthy, W. MacGillivray, and M. Standage, eds.), Brisbane, July 1991, p. 177.
[18] E. Weigold, Y. Zheng, and W. von Niessen, Chem. Phys. **150,** 405 (1991).
[19] X. Chen, Phys. Rev. A **49,** 1796 (1989).
[20] S. T. Hood, E. Weigold, I. E. McCarthy, and P. J. O. Teubner, Nature Phys. Sci. **245,** 65 (1973).
[21] E. Weigold, S. T. Hood, I. E. McCarthy, and P. J. O. Teubner, Phys. Lett. A **44,** 531 (1973).
[22] A. O. Bawagan, C. E. Brion, E. R. Davidson, and D. Feller, Chem. Phys. **113,** 19 (1987).
[23] L. C. Snyder and H. Basch, Molecular Wavefunctions and Properties, Wiley, New York 1982.
[24] D. Neumann and J. W. Moskowitz, J. Chem. Phys. **49,** 2056 (1968).
[25] R. Cambi, G. Ciullo, A. Sgamelloti, C. E. Brion, J. P. D. Cook, I. E. McCarthy, and E. Weigold, Chem. Phys. **91,** 373 (1984); **98,** 166 (1985).

[26] R. Pascual, I. E. McCarthy, and E. Weigold, 1987, unpublished.
[27] D. Feller, C. M. Boyle, and E. R. Davidson, J. Chem. **86,** 3424 (1987).
[28] C. E. Brion, S. T. Hood, I. H. Suzuki, E. Weigold, and G. R. J. Williams, J. Elec. Spectrosc. **21,** 71 (1980).
[29] A. O. Bawagan, R. Müller-Fiedler, C. E. Brion, E. R. Davidson, and C. Boyle, Chem. Phys. **120,** 335 (1988).
[30] C. L. French, C. E. Brion, and E. R. Davidson, Chem. Phys. **122,** 247 (1988).
[31] S. A. C. Clark, C. E. Brion, E. R. Davidson, and C. Boyle, Chem. Phys. **136,** 55 (1989).
[32] S. A. C. Clark, E. Weigold, C. E. Brion, E. R. Davisdon, R. F. Frey, C. M. Boyle, W. von Niessen, and J. Schirmer, Chem. Phys. **134,** 229 (1989).
[33] E. Weigold, K. Zhao, and W. von Niessen, J. Chem. Phys. **94,** 3468 (1991).
[34] A. L. Ritter, J. R. Dennison, and R. Jones, Phys. Rev. Lett. **53,** 2054 (1984).
[35] C. Gao, Y. Wang, A. L. Ritter, and J. R. Dennison, Phys. Rev. Lett. **62,** 165 (1989).
[36] J. Lower and E. Weigold, J. Phys. E: Sci. Instrum. **22,** 421 (1989).
[37] K. J. Nygaard, Yu Chen, J. Lower, P. Storer, and E. Weigold, Microsc. Microanal. Microstruct. **2,** 377 (1991).
[38] J. Lower, S. M. Bharathi, Yu Chen, K. J. Nygaard, and E. Weigold, Surface Science **251/252,** 213 (1991).